On the contact resistance between the anode and the porous transport layer in a proton exchange membrane water electrolyzer

Toni Srour, Kavita Kumar, Vincent Martin, Laetitia Dubau, Frédéric Maillard, Bruno Gilles, Jérôme Dillet, Sophie Didierjean, Bilal Amoury, Tien Dung Le, et al.

On the contact resistance between the anode and the porous transport layer in a proton exchange membrane water electrolyzer

Toni Srour[1], Kavita Kumar[2], Vincent Martin[2], Laetitia Dubau[2], Frédéric Maillard[2], Bruno Gilles[3], Jérôme Dillet[1], Sophie Didierjean[1], Bilal Amoury[1], Tien Dung Le[1], Gaël Maranzana[1]

1. Université de Lorraine, CNRS, LEMTA, F-54000 Nancy, France

2.Univ. Grenoble Alpes, Univ. Savoie Mont Blanc, CNRS, Grenoble INP, LEPMI, 38000 Grenoble, France.

3. Univ. Grenoble Alpes, Univ. Savoie Mont Blanc, CNRS, Grenoble INP, SIMAP, 38000 Grenoble, France

*corresponding author: gael.maranzana@univ-lorraine.fr

Abstract

The contact resistance between the anode catalyst layer and the titanium (Ti)-based porous transport layer (PTL) of a proton exchange membrane water electrolyzer (PEMWE) can limit the efficiency of the system and its durability. Generally, the PTL side in contact with the anode is coated with a precious metal, such as platinum. This results in an increased overall cost of the system. Here, we report on the influence of various metal coatings (400 nm coatings of platinum and gold; 2, 10, 400 nm coatings of iridium) on the beginning of life performance and on the durability of a PEMWE device. The durability tests included varying the voltage between 1.5 and 2.2V and between 0 and 2.2V with a total test duration of 510 hours by sample). The best beginning of life performances are obtained with a platinum coating but the best durability during start-stop events is obtained with a 10 nm iridium coating (representing less than 2% of the amount of iridium present in the system). The influence of the clamping stress is also evaluated. Whatever the nature of the coating, the electrical contact resistance decreases with an increase in the clamping stress and depends on the clamping history.

I. Introduction

The earth's temperature is rising at an increasing rate due to the excessive use of carbon-based fuels in energy production, and many countries are announcing measures to limit it to 1.5 °C. The International Energy Agency (IEA) has developed a net zero energy plan to increase the use of hydrogen (H_2) as a feedstock or energy carrier to 24 % of the final energy demand by 2050 [1]. H_2 must be supplied by low-carbon sources and water electrolysis coupled with renewable energies is a key element of this decarbonization plan. In recent years, proton-exchange membrane water electrolysis (PEMWE) has gained momentum for its flexibility and compactness. The bottleneck of this technology is its high cost per kW[2], mostly associated with the cost of electricity and of its constituting materials: platinum group metals (PGM) in the electrodes, Nafion proton-exchange membrane (PEM), titanium (Ti) in the porous transport layers (PTLs) and in the bipolar plates (BPs). The case of iridium (Ir) used to electrocatalyse the kinetically slow oxygen evolution reaction (OER) at the anode is emblematic as the largest contributor to the total overpotential of PEMWE cell is the OER kinetic overpotential. Moreover, Ir is a scarce and precious metal, and the Ir loading at the anode side still ranges between 1 and 3 mg cm^{-2}_{geo} ($\approx 0.7 g_{Ir}$/kW @ 70% efficiency). A large-scale development of the PEMWE technology therefore requires developing more efficient and more durable OER catalysts or tailored electrode formulations [3]–[14] so that the Ir loading per kW become lower than 0.01 g_{Ir}/kW. To achieve this objective, it is necessary to reduce the Ir loading per cm^2 of electrode, and to decrease the ohmic resistance of the membrane and interfacial contacts to reach higher current densities for a given efficiency. For example, switching from 1.5A/cm^2@1.8V to 3A/cm2@1.8V halves the Iridium loading per kW. Currently, 125 µm thick Nafion® 115 PEM is considered the best compromise between proton conductivity, H_2 crossover properties and durability. The development of thinner reinforced perfluorosulfonic acid (PFSA) membranes is underway [15]–[20], and will allow for increased current density at

the cost of increased H_2 permeation and lower durability. Less H_2-permeable materials such as hydrocarbon membranes [21] could partially solve the problem but have yet to prove their durability. A decrease of the electrical contact resistances between the different components of the assembly shall also lead to decreased Ir loading per kW. A case of particular interest is the contact resistance between the Ti PTL and the anodic catalyst layer. Because of the low pH and high potential conditions, this interface is subject to corrosion [22]. As shown by **Figure 1**, this contact resistance is the sum of three resistances [23] related to (i) the constriction of the current lines in the catalyst layer R_{cons}^{el}, (ii) the interface between the two layers R_{int} and (iii) the constriction of the current lines in the PTL. Since the electrical conductivity of the PTL is large, the constriction resistance in the PTL is negligible compared to the other two ones.

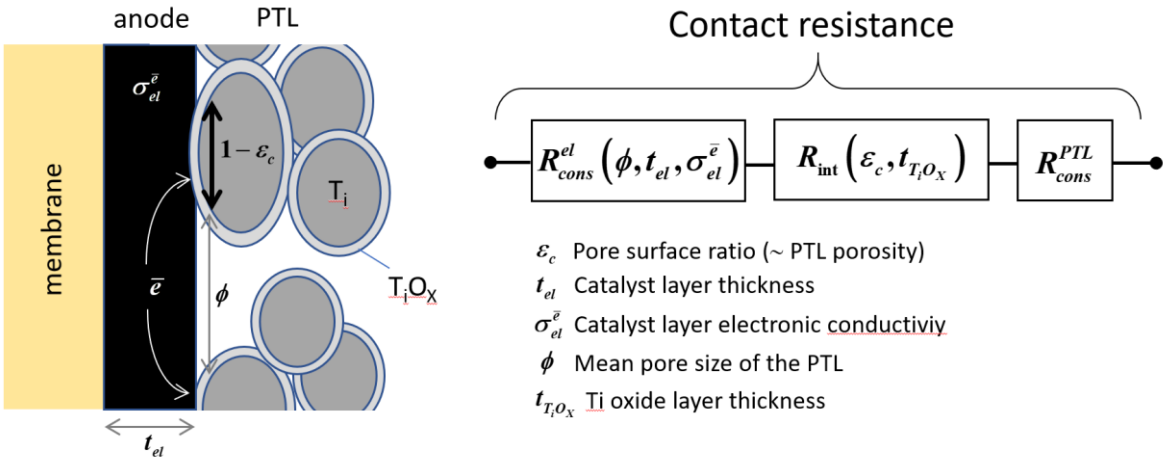

***Figure 1**. Electron transfer at the interface between the catalyst layer and the PTL. The average path travelled by the electrons in the catalyst layer is greater for PTLs featuring large pore size, yielding a constriction resistance.*

The constriction resistance in the electrode R_{cons}^{el} arises from the limited electrical conductivity of the electrode ($\sigma_{el}^{\bar{e}}$)[24], [25], and its value depends on (i) the size (ϕ) of the pores in the PTL, (ii) the thickness of the catalyst layer (t_{el}) and (iii) its electrical conductivity ($\sigma_{el}^{\bar{e}}$). An analytical expression of R_{cons}^{el} has been given by Parra-Restrepo *et al*. in Ref. [23]. Unfortunately, R_{cons}^{el}

increases when the Ir loading is decreased due to the micrometre-size of Ir oxide (IrO_2) particles used at the anode, and the resulting inhomogeneous and non-contiguous character of low-loaded anodes [25]. The interface resistance R_{int} depends on the percentage of the PTL surface in contact with the anodic catalyst layer: 1-ε_c (where ε_c is the percentage of PTL that is not in contact with the anodic catalyst layer. ε_c is typically of the order of the PTL porosity but its value depends on the clamping pressure) and on the thickness of the Ti oxide (TiO_x) layer forming at high anode potential (t_{TiOx}) as TiO_x is semi-conducting in nature:

$$R_{int} = \frac{t_{T_iO_x}}{\left(1-\varepsilon_c\right)\sigma_{T_iO_x}} \quad (1)$$

$\sigma_{T_iO_x}$ is the electrical conductivity of the titanium oxide.

Several strategies are possible to minimize the contact resistance between the anodic catalyst layer and the PTL:

(i) Using a PTL with small pores. As PTLs with very small pores lead to mass transport issues (the viscosity of water limits its transport by capillarity against the flow of dioxygen, O_2), [23] the optimal pore size thus corresponds to the best compromise between the constriction resistance and the mass-transport overpotential. The contact resistance can also be decreased without disturbing the water transport much by implementing a microporous layer (MPL) [26],[27],[28] between the PTL and the anodic catalyst layer. The tightening stress is another important parameter to control as high tightening stress forces the PTL to penetrate into the anodic catalyst layer, and thus reduces the average diameter of the pores (ϕ) located at their interface.

(ii) Maximizing the electrical conductivity of the anodic catalyst layer is also crucial for the proper functioning of a membrane-electrode assembly. However, the electrical conductivity of

materials at anode potential and under high oxygen pressure is generally poor, and can limit the use of supported Ir catalysts with low electrical conductivity [29].

(iii) Reducing the thickness of the TiO_x layer forming at the surface of the PTL in contact with the anode. To this goal, it is preferable to limit the maximum potential of the anode and/or to coat the surface of the PTL in contact with the anodic catalyst layer with an electron-conducting and durable material, such as a noble metal. This can typically be platinum (Pt) [30], gold (Au) [31], Ir [32] or niobium (Nb) [33], [34].Note that some of these metals also act as recombination catalyst between H_2 and O_2 [35].

(iv) Maximizing the contact between the PTL and the anodic catalyst layer (1-ε_c) to minimize the interface resistance. Experimentally speaking, this is achievable with increased clamping pressure or decreased porosity of the PTL. However, should the PTL be insufficiently porous, a mass transport resistance is generated. The effect of the clamping pressure will be discussed in detail below but it is mainly limited by the material strength, MEA durability, and the H_2 permeation.

Several studies have been conducted on the effect of clamping pressure on fuel cells' performance [36], [37] but only a few have investigated this for PEMWEs. Al Shakhshir *et al*. [38] have reported lower cell voltage and reduced H_2 cross-over at high clamping pressure (150 pound-force per square inch (PSI, translating into 1.3 MPa) on a 50 cm^2 PEMWE. Frensch *et al*. [39] conducted similar experiments on a 2.89 cm^2 PEMWE cell, and they varied the clamping pressure from 0.77 MPa to 3.45 MPa. No optimal value was observed but the PEMWE performance was improved with an increase in the clamping pressure, which the authors related to decreased contact resistance. Selamet *et al*. [40] tested the effect of the bolt torque on the contact resistance and PEMWE performance for different sealing gasket materials. They did not observe a clear optimum but from a certain clamping pressure the contact

resistance became constant. Borgardt *et al.* [41], [42] performed several clamping experiments and did not report any optimum. Surprisingly, with increasing clamping pressure, the cell voltage was found to decrease but, the mass transport losses and the H_2 crossover properties of the MEA were depreciated.

With the aim to reduce the interface contact resistance, in this work, we compare the benefits and the limitations of coating Ti PTLs with different metals (including Au, Pt, and Ir) and varying the clamping pressure. We assessed the electrical performance of the different cells and finely characterized the MEA materials before and after an accelerated stress test composed of potential variations between 1.5 and 2.2 V (slot aging protocol) and 0 and 2.2 V (start/stop aging protocol).

II. Materials and methods

II. 1. Description of the custom-made PEMWE cell

The schematic of the home-made PEMWE cell used in our experiments is represented in Erreur ! Source du renvoi introuvable..

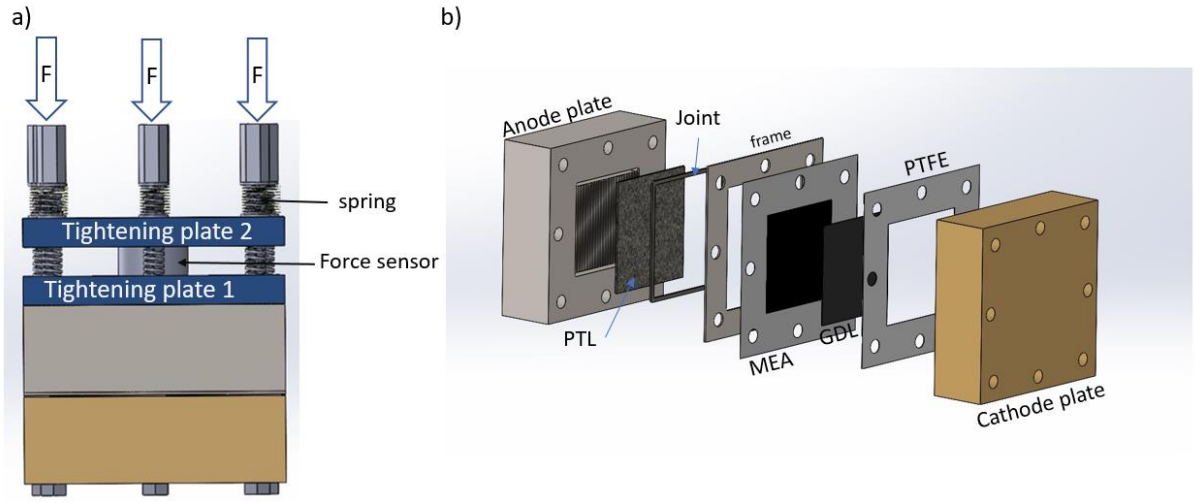

***Figure 2**. Representation of: a) the assembled view of the cell with the springs and the force sensor to accurately measure the force hence to deduce the clamping pressure (see **Figure S1**), b) an exploded view of individual components.*

The anodic plate is made from Grade 1 Ti, and comprises 25 straight channels in parallel. Their depth is 1 mm and they are 1 mm spaced apart from each other. The total flow area is 5 x 5 cm^2. The cathodic plate is made from stainless steel (316 L) subsequently coated with Wood nickel (1 µm) and Au (1.6 µm) to ensure a good contact with the 325 µm thick Toray 120 carbon paper gas diffusion layer (GDL). The cathodic plate is made of 25 straight parallel channels. Their depth is 0.7 mm and they are 1 mm apart. The anodic and cathodic plates are compressed via a system of 8 springs to limit the differential expansions due to the operating conditions (temperature and fluid pressure variations), and to keep a constant clamping pressure. The latter was measured thanks to a Burster 8438-6050 sensor. The total force applied is equal to the sum of the force applied on the active surface, the force applied on the Viton® gasket and the force exerted by the fluid pressure:

$$F_{CS} = F_J + F_{PTL} + F_F \quad (2)$$

Where F_{CS} (N) is the resulting clamping force measured with the Burster sensor, F_J (N) is the force applied on the Viton® gasket, F_{PTL} (N) is the force applied on the active area which the contact resistance depends, and F_F (N) is the force exerted by the pressure of the fluid ($F_F = PS_{PTL}$, with P the pressure of the fluid in the system). To know the clamping pressure on the active surface area, both the Viton® gasket and the Toray GDL should be characterized from a mechanical point of view (displacement as a function of stress) to calculate the compression ratio of the Viton® gasket and deduce F_J (see **Figure S2** and **Figure S3**).

The membrane electrode assembly (MEA) was purchased from IonPower. It comprises a Nafion® 115 PEM. The cathodic/anodic layer are composed of 0.3 mg PtC/cm² and IrO_2 powder, respectively. On the anode side, a 1 mm thick sintered powder Ti PTL with a porosity close to 37 % was used (Grade 1, from Top Star Non-ferrous Metals Co., Ltd, filtering 10µm). The PTL was used as received or coated with different metals. The coated side was placed in contact with the anodic catalyst layer. Soft 1.6 mm thick Viton® gaskets were used for the anode side sealing. It presses the membrane around the active surface which is supported by a non-deformable PTFE seal (150 µm) on the cathode side. An inox frame insulated with 40 µm Kapton sheets was used to keep the Viton® gasket in place, and to avoid its peripheral deformation.

II. 2. Physical vapour deposition on the PTLs

The PTL were coated with Ir using the magnetron sputtering technique[43] operating in the DC mode under an Ar pressure of 0.66 Pa with a 5 W plasma power. The growth rate (0.57 nm min^{-1}) was calibrated by depositing a thin layer on a silicon substrate using exactly the same operating conditions and the Ir thickness was measured using the X-ray reflectivity technique[44].

The Pt and Au coatings were prepared to the highest standards by the company Kerdry. The nature, the thickness and the equivalent metal loading of the coated-PTLs used in this work are presented in Erreur ! Source du renvoi introuvable.. The native PTLs were also coated with Ir (400 nm, 10 nm, or 2 nm), with Au (400 nm) or with Pt (400 nm). As shown in **Figure S4**, the characteristic pore size is significantly greater than the thickness of the metal coating, and, as a result, it is not obstructed by the coating.

Coating	Coating thickness (nm)	Metal loading (mg.cm^{-2})
No coating (Ti PTL)	-	-
Ir	400	0.9
Ir	10	0.02
Ir	2	0.004
Pt	400	0.86
Au	400	0.78

Table 1: Characteristics (nature, thickness and the equivalent metal loading of the coated PTLs used in this work.

II. 3. PEMWE cell hardware

Before each experiment, the PTLs were cleaned by ultrasonication in an acetone solution for 25 min, and then rinsed with ultrapure water for 25 min in the same ultrasonic bath. The GDLs, the PTFE seal and the Viton® gasket were subsequently rinsed with an ethanol solution for 25 min and then rinsed with ultrapure water. The components were then dried in vacuum for one hour at 80°C. The assembly was made with the dry membrane, balanced with the ambient humidity. The cell was then integrated in the test bench shown in Erreur ! Source du renvoi introuvable.. Two identical water circulation loops are implemented for the anode and cathode. The temperature of the plates is regulated by a circulation bath controlled by a Pt probe inserted in the anode plate. The water flow is also thermalized thanks to two heat exchangers before the anode and cathode inlet, in order to obtain performances independent of the water flow rate.

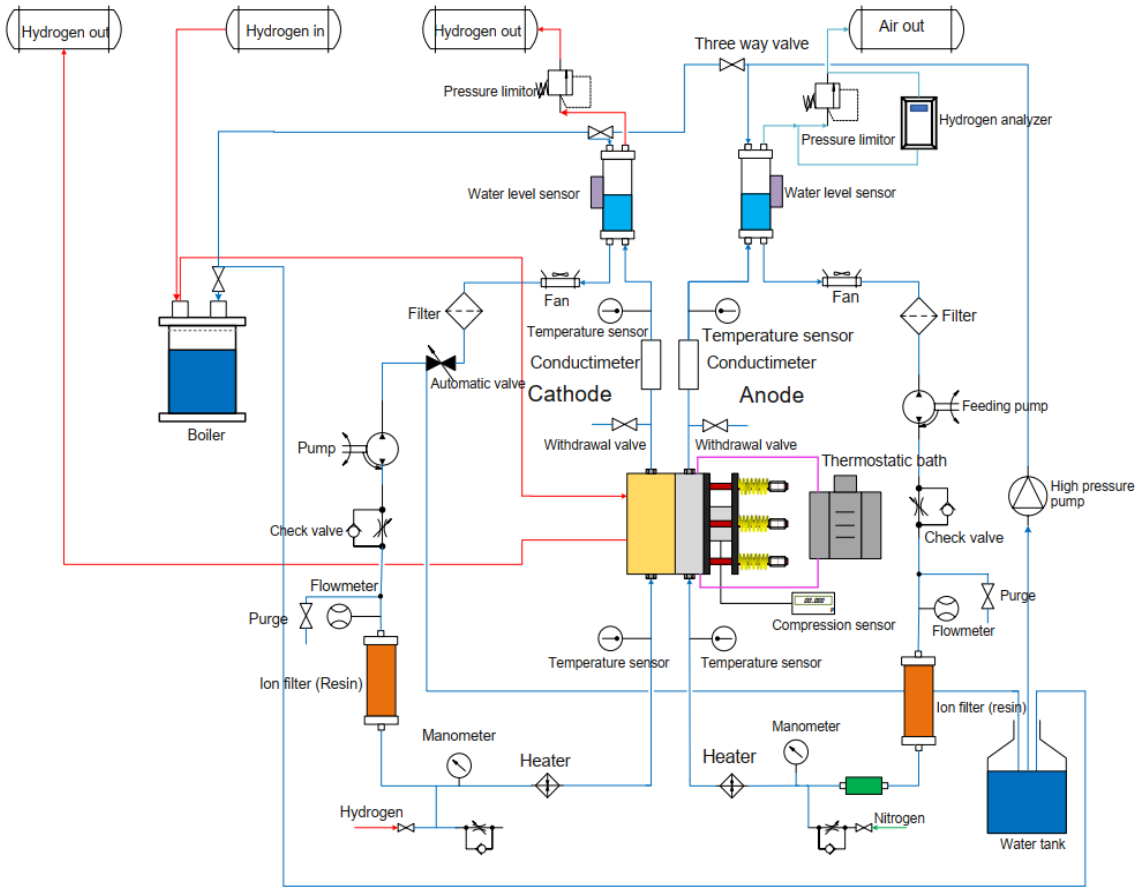

***Figure 3**. Schematic diagram of the experimental test bench at LEMTA.*

The water temperature is measured at the inlet and at the outlet of the two compartments. The water conductivity is measured at the outlet of the two compartments and the H_2 concentration in O_2 is measured at the anode outlet thanks to a KEATON K1550 hydrogen sensor, just after drying the O_2 flow. The bench is fully automated thanks to a LabVIEW® program to ensure the reproducibility of the tests and to carry out aging tests 24 hours a day, 7 days a week. An ion-exchange cartridge (AMBERLITE MB20) was used to get rid of cationic impurities. Water exiting the anodic and cathodic compartments was sampled at the exit of the cell. The sampled volume was compensated with ultrapure Milli-Q EQ 7000 grade water with resistance close to 18.2MΩ.cm in order to maintain a constant water volume of 10mL.

Note on the variability of results: the variability of experimental measurements is linked to the measurement error itself (sensor accuracy), or to the reproducibility of experiments.

With regard to the first point, we stress that cell voltage and current measurements are highly accurate, and that the associated error bars are very small, if not negligible. Measurement variability due to test reproducibility, on the other hand, can be estimated by performing the same measurement several times and calculating the standard deviation of the results. However, due to time and budget constraints, these multiple tests were not conducted. Variability therefore essentially depends on the quality of the materials used and on the control of the boundary conditions imposed on the cell (temperature, flow rates, water quality, clamping pressure, etc.). In this work, we have taken precautions to ensure precise and repeatable control of these boundary conditions - see bench diagram:

- The water conductivity was monitored online on both the anode and cathode sides to ensure optimal water quality.

-The clamping force was precisely controlled (± 10 N).

-Inlet temperatures on the anode and cathode sides were controlled by two highly efficient heat exchangers with a repeatability of ± 0.5 °C. These water temperatures at the inlet and outlet were measured by four calibrated thermocouples (± 0.2 °C).

-Plate temperatures were controlled by a thermal bath associated with a platinum probe to reach an accuracy of ± 0.1°C.

-Pressures were controlled by two pressure controllers (± 10mBar).

As regards to the variability of the materials used, all tests were carried out with MEAs purchased from well-established manufacturer (Ionpower) and issued from the same batch. Toray's GDLs are renowned for their quality, and Ldafilter's PTLs were also all from the same batch. All these precautions ensured minimal variability, even though these couldn't be precisely quantified. As shown in **Figure S5**, the variability between polarization curves is

insignificant for current densities below 2.5A/cm^2 but becomes pronounced at higher current densities. This variability is attributed to the characteristics of the materials involved rather than the boundary conditions imposed on the cell.

II. 4. PEMWE operation

Break-in

After 2 hours of water circulation and warming up, the cell was operated for one hour at 1A/cm^2, at 60°C and at atmospheric pressure. Then, a polarization curve was measured, the pressure in both compartments was adjusted to 15 bars, and the preceding steps repeated. The temperature was then set to 80°C and all the previous steps were again repeated. At the end, the break-in period is 48 hours in total.

Polarization curves and electrochemical aging spectroscopy (EIS)

The current density was increased from 0.25 A steadily till 1 A with 0.25 A steps, then from 1 A to 2 A with 0.5 A steps; next from 5 A till 50 A with 5 A steps, and finally from 50 to 140 A (5.6A/cm²) with 10 A steps. Then the current was decreased following the same steps. The plotted cell voltage is the average of the voltage measured during the increasing and decreasing current ramps. To obtain a homogeneous cell temperature, the duration of each step was 20 min. After each current density step, an electrochemical impedance spectroscopy (EIS) measurement was performed with an amplitude of 25 % for current densities less than 10 A and 10 % for current densities higher than 10 A. The frequency range was from 100 mHz to 10 kHz. The impedance was averaged between 1 kHz and 4 kHz to obtain the plotted high frequency resistance (HFR).

Two AST protocols were carried out successively.

Slot aging protocol

The slot aging protocol comprises cell voltage steps between 1.5 V (5 min) and 2.2 V (5 min), and lasts for 340 hours in total. Polarization curves and electrochemical impedance spectra were measured every 24 hours. This aging test was realized using a pressure of 15 bars, a temperature of 70°C, and a clamping pressure of 5.1 MPa. A constant water flow rate of 10 L/h was used to feed the anodic and cathodic compartments.

Start-stop aging protocol

During this protocol, following the slot aging protocol, the electrolyzer was repeatedly started and stopped using an excess of H_2. By stopping the anode water pump and keeping the cathode one functioning, all the O_2 dissolved in the anode compartment recombined with crossover H_2, leading to a drop of the anode potential to a value close to 0 V [45]. The cell was operated at a constant voltage of 2.2 V for 30 min, then it was stopped for 30 min. Similar to what was done for the slot aging protocol, polarization curves and electrochemical impedance spectra were measured every 24 hours. This test was conducted at 1 bar to keep the concentration of O_2 dissolved in water to a low value. The operating temperature as 70°C and the flow rates at each electrode was 10 L/h. The total duration including the characterization steps was 170 hours.

II. 5. Scanning Electron Microscopy (SEM)

A field-emission-gun scanning electron microscopy (FEG-SEM, Zeiss Gemini 500 microscope) was used to acquire the scanning electron microscopy (SEM) images. The microscope was equipped with both a secondary electron detector and a backscattered electron one and it was developed to image electrons at low accelerating voltage (usually at or below 15 kV), which is required for polymer-containing materials such as MEA. The samples consisted of square zones cut in the MEA and the observations were made at the cross-sections. The samples were prepared by first embedding the MEA in Epoxy® resin, drying them in ambient

air for one day, polishing them with a SiC polishing disk with a small grain size (4000), and finally covering them with a thin carbon film. The images were statistically analysed to estimate the thicknesses of the PEM and of the anode and cathode catalytic layers.

II. 6. Inductively-coupled plasma mass spectrometry measurements

The elemental composition of the water sampled from anode and cathode compartment was determined using a PerkinElmer NexION 2000 ICP-MS. Rhodium (Rh) was used as ICP-MS internal standard (2.5 µg L^{-1} solution). Five-point calibration curves were obtained using a blank and prepared standard solution containing ^{195}Pt, ^{197}Au, ^{193}Ir, ^{48}Ti, ^{60}Ni, ^{98}Mo, ^{56}Fe and ^{52}Cr at concentrations of 0, 5, 10, 20 and 50 µg/L. These solutions were freshly prepared using monoelement ICP standard solution (1000 mg L^{-1}, Carl Roth GmbH) and a 0.27 mol/L HNO_3 solution.

III. Results and discussions

Effect of the various surface coating on the beginning of life performance

Erreur ! Source du renvoi introuvable.**a** shows the polarization curves recorded with metal-coated and uncoated PTLs at the beginning of life (BoL), just after the break-in procedure. The BoL performance gain arising from the metal coatings is obvious. Indeed, whereas all metal-coated PTLs performed similarly below 2A/cm^2 (slightly better with the Pt-coated PTL), PGM-coated PTL clearly outperformed above 2A/cm^2 (though a certain dispersion of the electrical performances was observed).

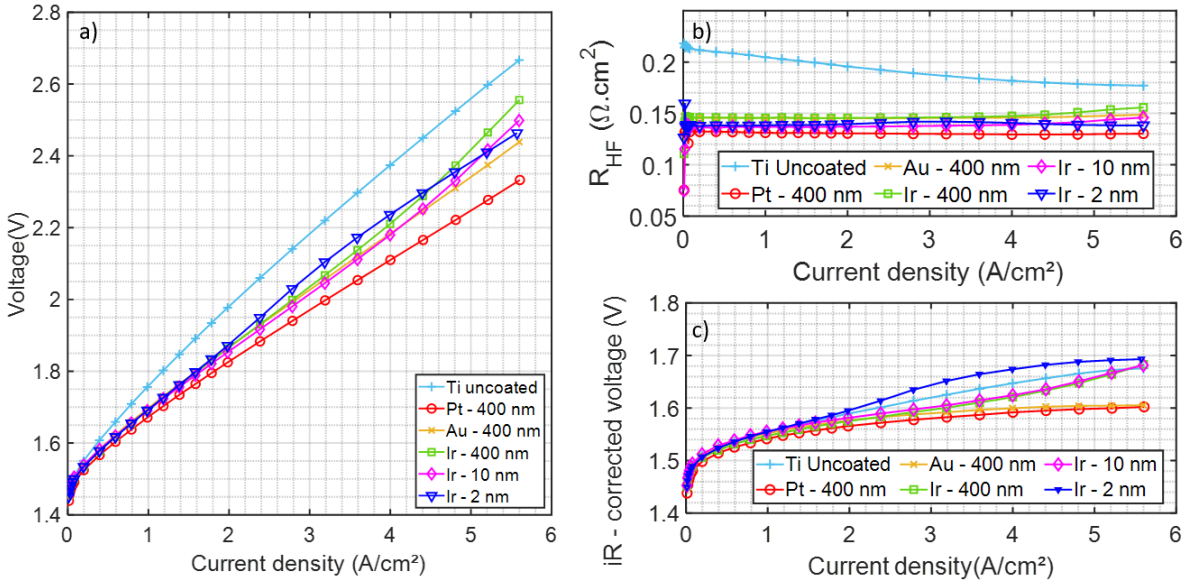

Figure 4*. a) Polarization curves at the beginning of life for the different coated and uncoated PTLs. P_{H2}=P_{O2}=1bar. T=70°C. Water flow rates = 10l/h. Clamping pressure = 5.1 MPa. b) Corresponding high frequency resistances, c) IR corrected polarization curves.*

As shown in **Figure 4b**, the gain in cell voltage for metal-coated PTLs mostly arises from a 30 % reduction of the HFR value (Pt 400 nm < Ir 400nm ~Ir 10nm ~ Ir 2nm ~ Au 400 nm). Note also that the HFR value recorded with a bare (uncoated) Ti PTL was almost two times higher than that of the PGM-coated PTLs but decreased as a function of the current density. This effect can be rationalized by considering the higher PEM temperature encountered when an uncoated Ti PTL is being used (thermal contact resistance between the PTL and the anode, higher heat released). Besides, we noticed a mild increase of the HFR value and of the cell voltage at current densities exceeding 4 A/cm^2 for Ir-coated PTLs (**Figure 4a**, **Figure S5** and **Figure S6**). The iR-corrected polarization curves displayed in **Figure 4c** confirm that a deviation from the expected exponential trend is observed above 2A/cm^2 for the Ir-coated Ti PTLs at the BoL. This mass-transport overvoltage progressively decreased over time (refer to Erreur ! Source du renvoi introuvable. and **Figure S5** and **S6**). This phenomenon was explained by taking into account the low wettability of the metallic Ir coatings, which may progressively diminish as they undergo oxidation [46] [47]. The same effect occurred on the Au-coated Ti

PTL, although to a less extent. Importantly, and contrary to common beliefs, there was no gain of cell voltage associated with Ir-coated PTLs because only a fraction of the Ir atoms are in contact with the ionomer of the anodic catalysts layer, and thus catalytically active. This result suggests that the amount of Ir required to coat the PTLs could possibly be reduced, hence different Ir coating thickness were prepared and tested in the rest of the work.

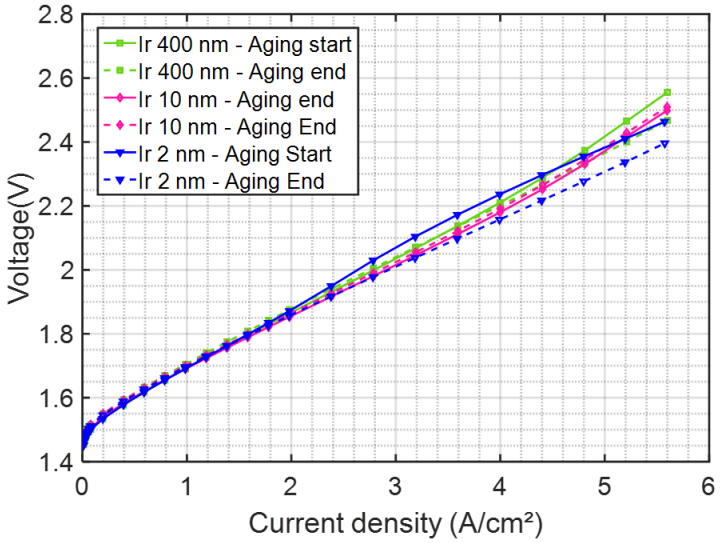

***Figure 5**. Polarization curves at the start of the slot aging and 340 h later for the different Ir coatings. The mass-transport issue observed at 2A/cm^2 has partly disappeared.*

Effect of the clamping pressure at the beginning of life

Erreur ! Source du renvoi introuvable.**a** shows the polarization curves for the uncoated and Pt-coated PTLs at different clamping pressures. The corresponding HFRs as a function of the current density are displayed in Erreur ! Source du renvoi introuvable.**b** and its variation as a function of the clamping pressure is shown in **Figure 6c**. As expected, an increase in the clamping pressure leads to a reduction of the contact resistance, certainly due to a larger contact surface between the two layers (1-ε_c term), and this hypothesis is supported by the fact that the gain does not depend on the nature of the metal coating. As shown in **Figure 6c** and **Figure S7,** for these state of the art materials, the average gain - or the average sensitivity of the high frequency resistance to the clamping pressure- is of the order of 3mΩ.cm^{2}MPa^{-1}. Because the

maximum clamping pressure was limited by the Toray GDL (a rather soft material) in our experimental set-up, no optimum of clamping pressure was observed.

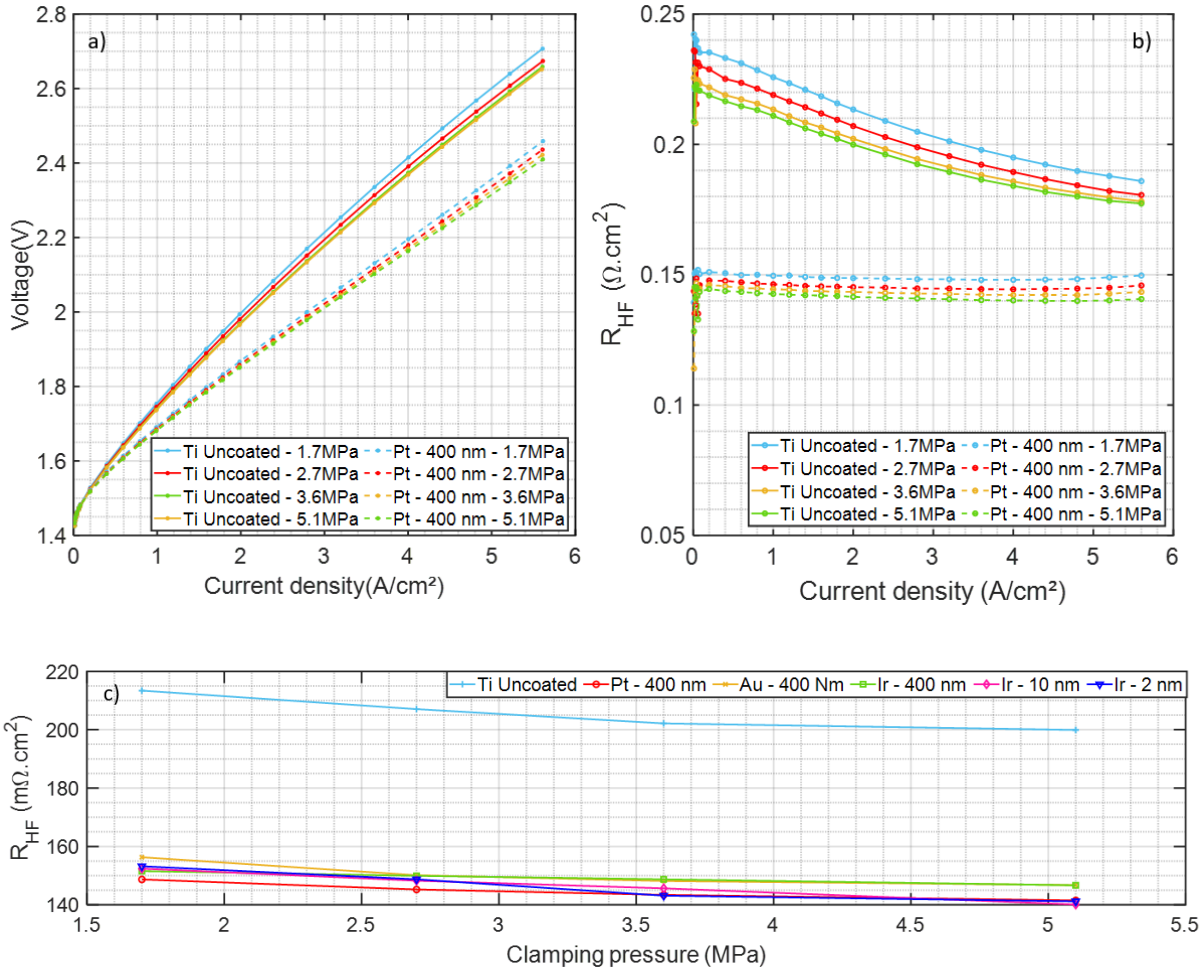

Figure 6*. a) Polarization curves at the beginning of life for the Pt-coated and uncoated PTLs for different clamping pressures.* $P_{H2}=P_{O2}=1$ *bar. T =70°C. Water flow rates = 10 l/h, b) the corresponding high frequency resistances and c) the HFR variation in function of the clamping pressure @2A/cm² to measure its sensibility to clamping.*

Accelerated stress tests

The ASTs were carried out using a clamping pressure of 5.1 MPa. **Figure 7a** displays the cell voltage at 2A/cm² as a function of the aging time. The corresponding HFR values measured by electrochemical impedance spectroscopy are displayed in Erreur ! Source du renvoi introuvable.**b**. We first note that the HFR and the cell voltage rapidly increased during the slot aging protocol for the uncoated and Au-coated PTL, but not for the Ir- or Pt-coated ones. During

the start/stop aging protocol, the HFR of the uncoated PTL first increased, before reaching a maximum after 40 hours of aging. The HFR value then decreased again and stabilized during the rest of the AST. Both the HFR and the cell voltage recorded with other metal-coated PTLs were pretty stable during the start/stop aging protocol, one exception being observed for the 2 nm Ir-coated PTL. In **Figure 7c** and **d**, the conductivity of the water measured at the anode and cathode outlets shows no major difference between samples. It is slightly higher for the 10 nm Ir coating at the cathode outlet following the start/stop aging protocol, a trend that unfortunately we would not explain.

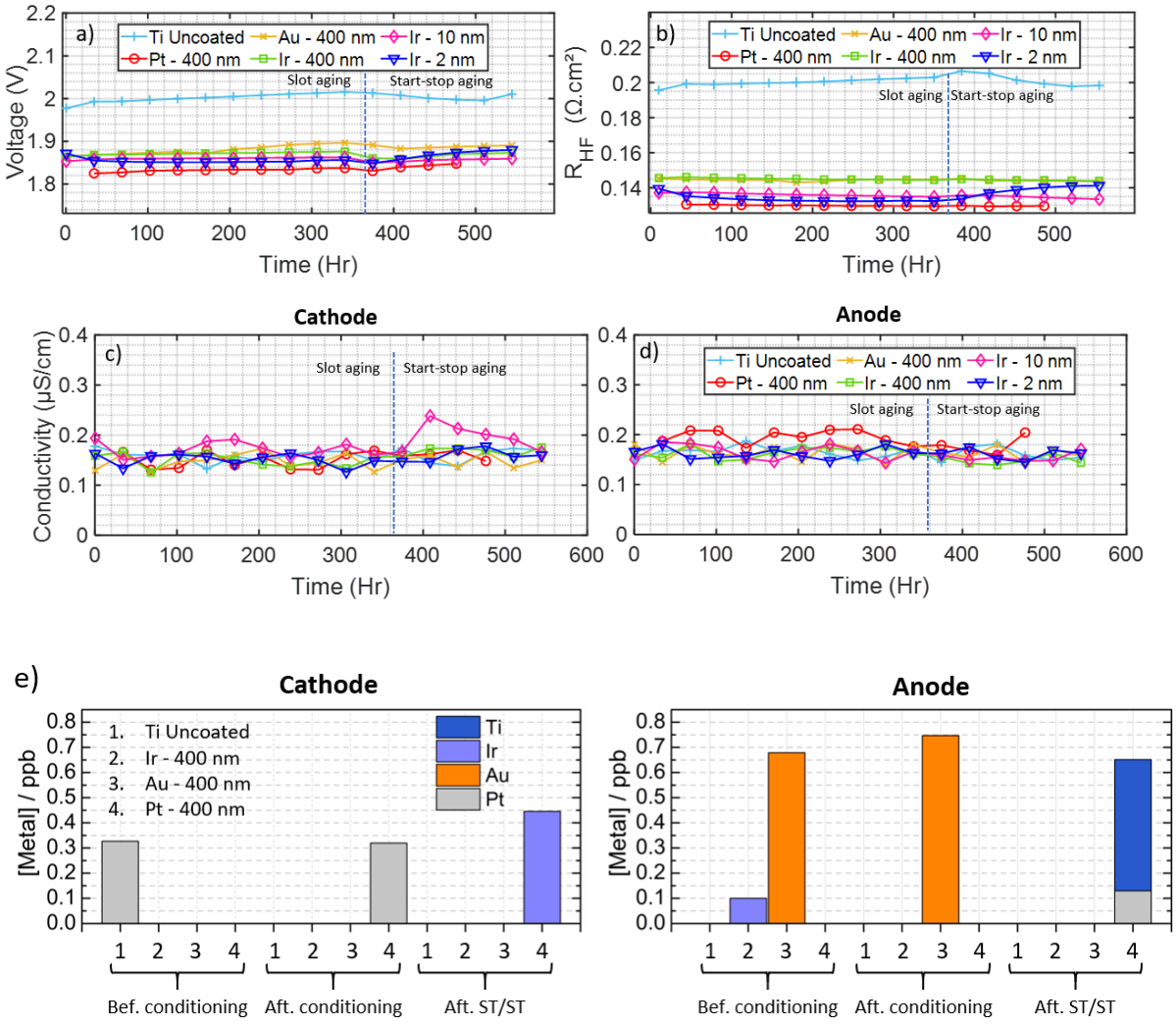

***Figure 7**. a) Cell voltage @2A/cm² as a function of aging time. P_{H2}=P_{O2}=15 bars (slot aging)/1bars (start-stop aging. T=70°C. Water flow rates = 10 l/h. Clamping pressure =*

5.1Mpa. b) the corresponding high frequency resistances and c) Water conductivity as a function of aging time for the i) anode side and ii) the cathode side, e) Ir, Pt, Au and Ti amounts detected in the anode and cathode water lines after different life stages.

To rationalize our results, we first refer to the Pourbaix diagrams [48]of the coating metals in pH ≤ 1 liquid water. The Pourbaix diagram of the Ti-water system indicates that Ti anodically dissolves for potential exceeding -1.21 V *vs*. the standard hydrogen electrode (SHE) before forming a non-stoichiometric TiO_2 film above -0.66 V *vs*. SHE. It can thus be assumed that, during the slot aging protocol, the uncoated regions of Ti PTLs become covered by a TiO_2 layer, which thickens continuously (the TiO_2 film thickness increases linearly with potential and its rate follows an inverse logarithmic law with time - 1/film thickness = f[ln(*t*)][49]). The Pourbaix diagram of the Au-water system indicates that Au is continuously dissolved into Au^{3+} ions for potentials exceeding 1.498 V *vs*. SHE, *i.e.* in the conditions of the slot aging protocol. On the contrary, Pt and Ir are known to form insoluble oxides at PEMWE anode potentials but their reduction at potentials approaching 0 V *vs*. SHE leads to release of dissolved Pt [50], [51]and Ir [52] cations in solution by a so-called place-exchange process.

These thermodynamic bases being established, we first discuss the case of uncoated Ti PTLs. We first note that the increase of the HFR value and of cell voltage recorded as a function of time for uncoated Ti PTLs (**Figure 7a** and **Figure 7b**) agrees with former findings of Rakousky *et al*. [53]and Lædre *et al.* [54]. The authors proposed that high PEMWE anode potentials cause passivation of the surface of the Ti PTL (formation of TiO_2), and that periodic excursions to low electrode potential, such as those experienced during the start/stop protocol, partially reduce the build-up of the TiO_2 film. The Pourbaix diagram of Ti, which shows that TiO_2 is unlikely to reduce at 0 V *vs*. SHE, put into question this scenario. The reduction of the TiO_2 during the start/stop protocol also cannot explain the bump observed in the HFR *vs*. time curve and the cell voltage stabilization during the start-stop aging protocol. To rationalize our findings, we stress that Williams *et al*.[55] have reported that TiO_2 films dissolve chemically to form

Ti(IV) species in solution, and that the rate of TiO_2 dissolution is first order in proton concentration in solutions of low pH. Moreover, the authors observed that a mild cathodic polarization facilitates the dissolution of the TiO_2 film [47]. The observed bump in the HFR value and the stabilization of the cell voltage during the start/stop aging protocol may thus reflect the dissolution of the TiO_2 layer formed on the uncoated Ti PTL and the regeneration of a "fresh" Ti surface during the stop events.

We now discuss the case of the PGM-coated PTLs. As discussed above, thermodynamics indicate that the Au coating is likely to be dissolved into Au^{3+} ions during the slot aging protocol. The released Au^{3+} ions thus redistribute within the whole MEA, and redeposit electrochemically within the anode or the anodic PTL during the stop events. A fraction of the released Au^{3+} ions is also likely to diffuse inside the PEM, where they will be reduced by crossover H_2 (at a certain distance of the anode, the atmosphere becomes richer in H_2 than in O_2, and this causes the chemical reduction and the precipitation of Au^{3+} ions in the PEM). Accordingly, it was no surprise to observe Au nanoparticles in the aged PEM after the ASTs (**Figure 8e** and **Figure 8f**).

According to the Pourbaix diagram of the Ir-water system, Ir form oxides in the experimental conditions of the slot aging protocol, and such Ir oxides are partially reducible during the stop events [52]. The released Ir cations may then redeposit at the PTL surface or in the anodic catalyst layer during the start/stop ageing protocol. The slight increase of the cell voltage observed for the 2 nm- and 10 nm-Ir coated PTLs suggests that not all Ir cations redeposited at the PTL surface in contact with anode during the start/stop ageing protocol, leading to some regions of the PTL becoming uncoated. In contrast, no change of the HFR value and of the cell voltage was observed when a 400 nm Ir-coated PTL or a 400 nm Pt-coated PTL was used. Which PTL coating is optimal for the PEMWE application remains an open question. The conductivity and the chemical analysis of the water sampled at the anode and cathode provide

us with partial answers. Indeed, the higher conductivity of the water sampled at the anode for the PEMWE device using a 400 nm Pt-coated PTL compared to that using a 400 nm Ir-coated PTL suggests that Ir might be more robust than Pt. This hypothesis is supported by the ICP-MS analysis of the water sampled from the anode and cathode compartments after the break-in: Pt was detected in the water sampled at the cathode, not Ir. However, this statement must be qualified since the Pt concentration was extremely low (0.3 ppt) and since traces of Pt were noted in the water before conditioning for the experiment using an uncoated PTL, most likely due to imperfect rinsing of the water lines. Also, both metals were detected in the water sampled from the cathode (Ir) or from the anode (Pt) during the start/stop aging protocol (**Figure 7e**). The answer to this question therefore lies in the operation mode of the PEMWE device. Should the PEMWE system be operated continuously or be shut down in a controlled manner so that the anode potential does not reach 0 V *vs*. RHE, an Ir-coating seems to be a better choice. Moreover, as a 10 nm Ir-coating represents 0.02 mg_{Ir}/cm^2, *i.e*. only a 2% increase of the total Ir loading, coating the PTL with Ir may thus enable durable operation at high current densities/cell voltages as required by the H_2-market. Should the PEMWE be operated intermittently, both metals are likely to be corroded and redistributed in the MEA. As both IrO_2 and PtO_2 are good OER catalysts (and Ir and Pt good HER catalysts), any metal/metal oxide redeposition in one electrode should yield a negligible catalytic penalty. In view of the current 7 to 8-fold lower price of Pt *vs*. Ir, we suggest Pt as the optimal choice for PTL coating in this operation mode.

To support our findings, the PEMWE cells were also disassembled after the ASTs and the MEAs and the anodic PTL materials were examined with SEM. **Figure 8a-d** shows optical images of the PTLs after disassembly. Black and clear stripes corresponding to regions of the anodic layer which remained stuck under the rib are clearly visible. This signs heterogeneity of the clamping stress at the rib-channel scale, mostly because the carbon GDL used at the cathode was not rigid enough to homogenize the clamping stress. **Figure 8e-f** shows the SEM images

of the MEA associated with the Au-coated PTL are in agreement with what was discussed above, the Au coating appeared partially dissolved and Au nanoparticles were found in the PEM or at the PEM | anode catalyst layer. For other coatings, on the contrary, no elemental trace was noted, either in then ionic or nanoparticulate form.

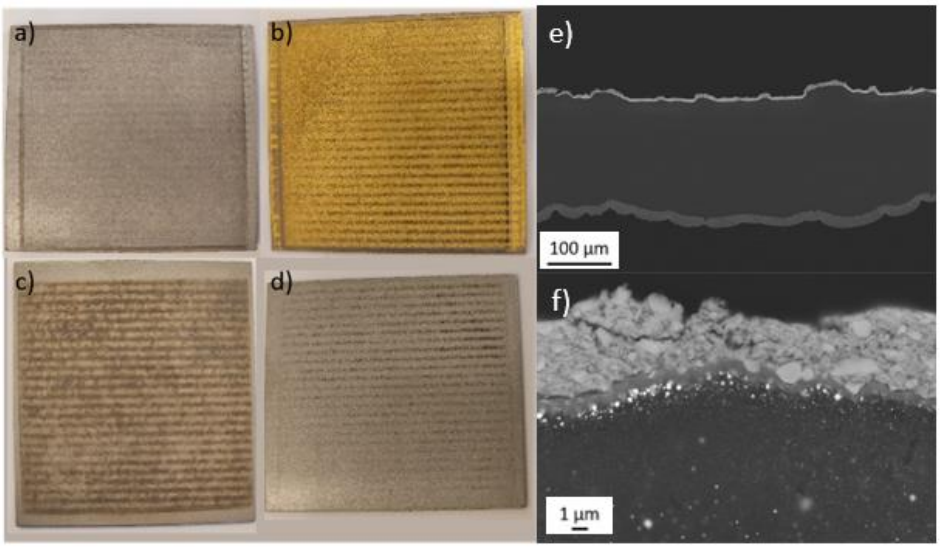

Figure 8*. Photographic images of the aged PTLs which show the difference between the dark and light bands. In the following order: a) Ir coated PTL, b) gold coated PTL, c) uncoated PTL, d) platinum coated PTL. SEM Images of the MEA e) and the anode side f) for PTL coated with Au.*

SEM images of the different MEAs before and after aging are displayed in **Figure 9**. We note some scatter in the thicknesses of the PEM and of the cathodic and anodic catalyst layers, probably causing small variations in the BoL performance. In agreement with former findings

[53], [56], [57], a decrease in the thickness of the anodic catalyst layer was observed. In view of the limited duration of the aging test, we ascribed this result to a change of its porous structure.

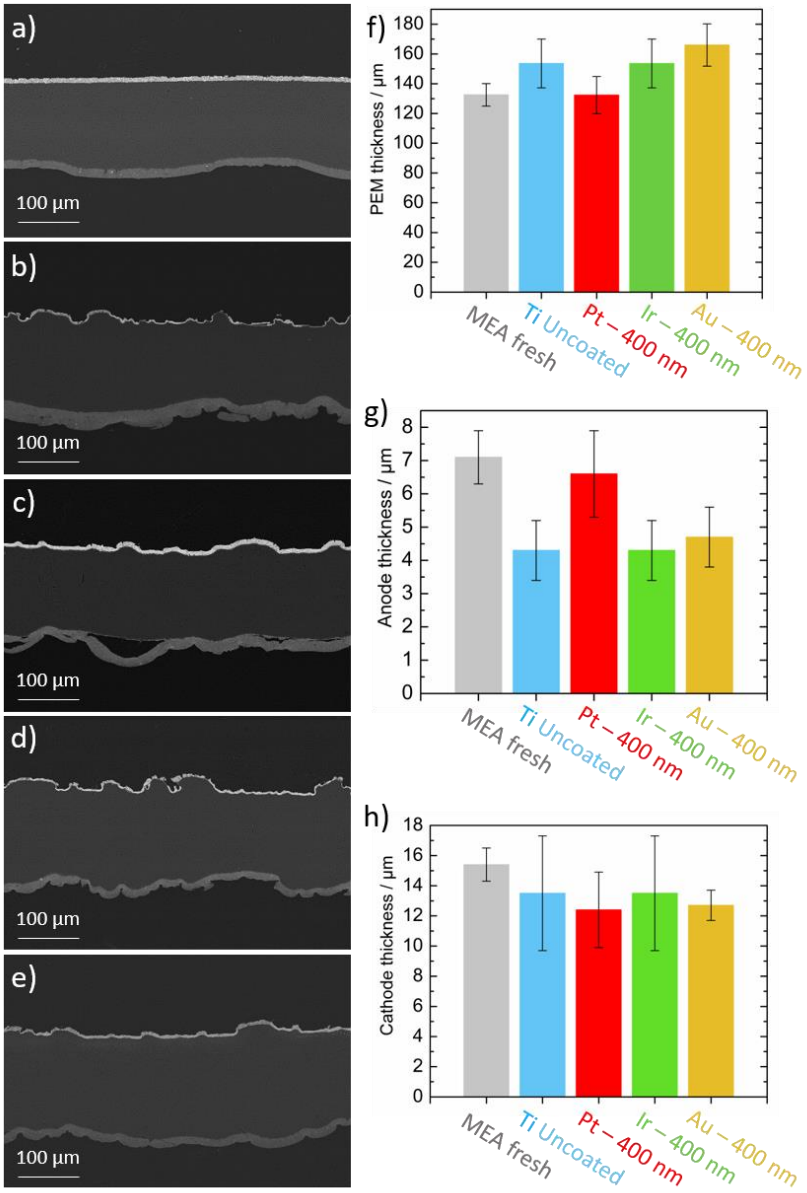

***Figure 9**. (a-e) SEM images of the MEAs, (f) estimation of the thicknesses of the PEM and (g, h) of the anodic and cathodic catalyst layers after the aging procedure, respectively.*

Higher clamping pressure and effect of the clamping history

Finally, we aim at finding whether an optimum in the clamping pressure can be obtained. To increase the tightening force, larger diameter bolts were used and the cathodic Toray GDL was

replaced by a PTL in platinized Ti fibers (Bekaert) with a thickness of 500 µm (at the anode, an uncoated Ti PTL was used). The thickness of the PTFE gasket was adjusted to guarantee tightness. The clamping pressure was first increased to 11.2 MPa, before being reduced to a minimal pressure, *i.e*. 1.7 MPa, then increased again to 8.2 MPa, then reduced again to 1.7 MPa.

Erreur ! Source du renvoi introuvable.**10** shows the four phases of the clamping pressure test. During the first clamping phase (from 1.7 to 11.2M Pa - blue curve), the potential decreased from 2.02 V to 1.90 V. This increase in cell performance was explained from the increase in the contact points between the catalyst layer and the PTL (increase of $1-\varepsilon_c$) and the consequent decrease in constriction resistance. Surprisingly, the cell performance further improved when the clamping pressure was reduced (from 11.2 to 1.7 MPa – red curve). The HFR and the cell voltage decreased (Erreur ! Source du renvoi introuvable.**10a** and **Figure 10c**) until an optimum clamping pressure of 3.7 MPa then increased again upon further reduction of the clamping pressure. One explanation could be that the high tightening established an intimate contact between the PTL and the electrode, such contact being irreversible insofar as a relaxation of the constraint does not disturb it. The relaxation of the constraint, on the other hand, can increase the water content in the PEM (by relaxation of the visco-elastic constraints) and therefore its proton conductivity, accounting for the better electrical performance. The variation of the permeation rates during this test (Erreur ! Source du renvoi introuvable.**b**) supports this hypothesis. Indeed, it is well documented that the gas permeability coefficient of Nafion increases with the water content[58]. The second tightening up to 8.2 Mpa further compressed the PEM without improving the contact resistance, accounting for no change of the HFR value.

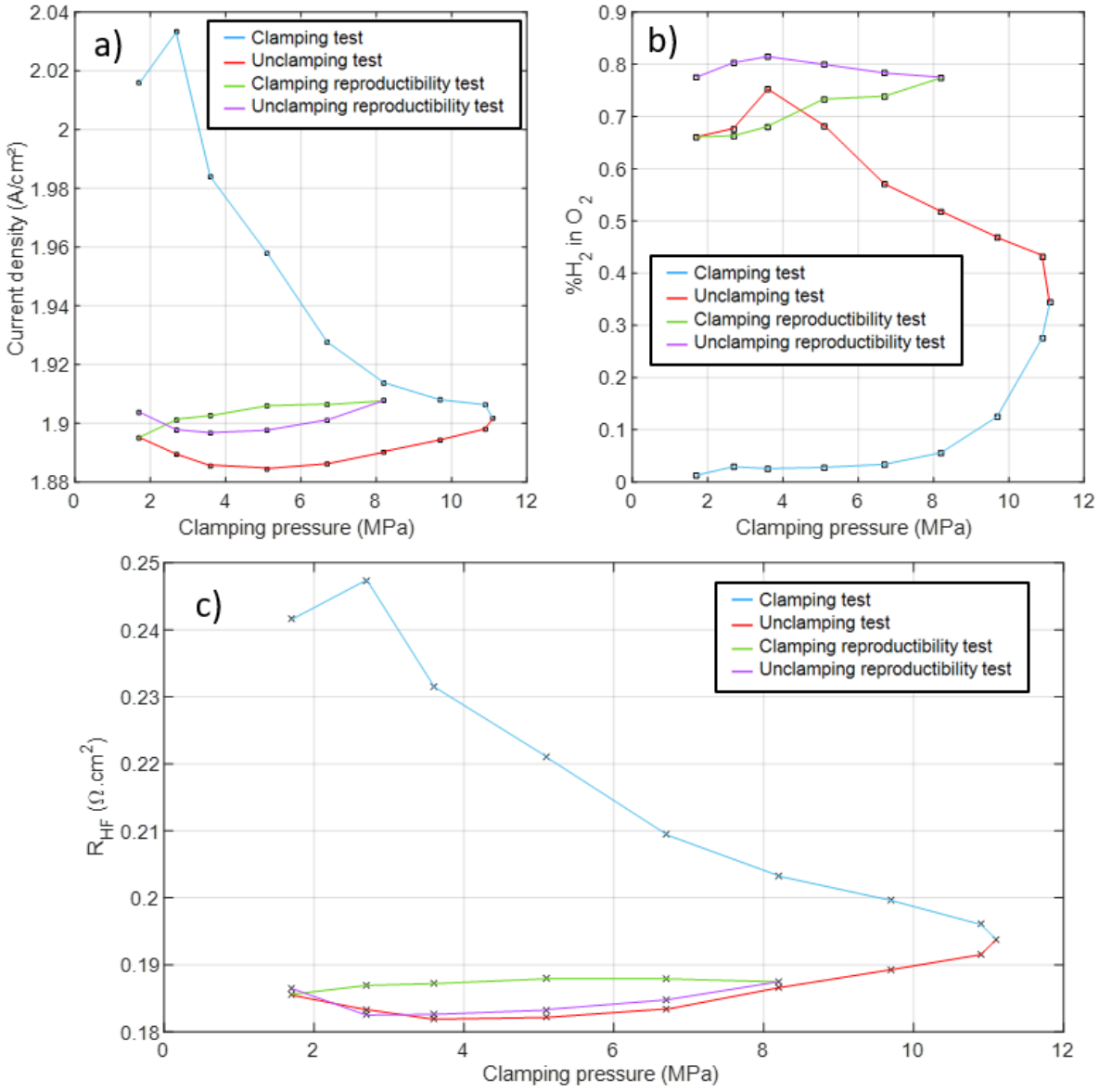

***Figure 10**. Effect of the clamping pressure and of the clamping pressure history. Uncoated PTL P_{H2}=P_{O2}=1 bar. T=70°C. Water flow rates = 10 l/h. a) Cell voltage @2A/cm^2. b) Corresponding hydrogen concentration in oxygen curves. c) corresponding high frequency resistance curves.*

A second relaxation of the stress slightly improved the cell performance for an optimal stress of the order of 2.4 MPa but the doubly-pressurized MEA performed worse than the simply-pressurized one. We thus conclude that the optimal clamping pressure for our setup is

comprised between 2.4 MPa and 3.7 MPa but that an initial tightening to 11 MPa is required for optimal PEMWE cell performance. It remains to be seen whether this optimum is sustainable over time, during aging. The significant increase in gas permeation, which is not reversible either, is a critical point.

IV. Conclusion

The electronic contact resistance between the anodic catalyst layer and the PTL negatively affects the PEMWE cell performance over time. Indeed, under the harsh conditions of a PEMWE anode (high potential, low pH and high oxygen pressure), a Ti oxide film builds up, increasing the series resistance and decreasing the energy efficiency of the PEMWE system. The contact resistance depends on the properties of the PTL (pore size, porosity, on the presence/absence of surface coating), on the properties of the anode electrode (electronic conductivity and thickness) and on the clamping stress. It is not intrinsic to the PTL and can be minimized provided the electrode, the membrane, and the oxygen pressure are considered. In this study, we compared the effect of different surface coatings on the performance of a PEMWE cell before and after a 550 h accelerated ageing test composed of potential variations between 1.5 V and 2.2 V (slot aging protocol) and between 0.0 V and 2.2 V (start/stop aging protocol). The MEA was composed of Pt/C and IrO_2 at the cathode/anode, respectively and of a Nafion 115 membrane. A 30 % reduction of the HFR value was noticed when PGM-coated PTLs were used. A Pt surface coating on the PTL yielded the best beginning of life performance. However, it turned out to be slightly less stable compared to an Ir surface coating, particularly during the slot aging protocol. A 10 nm Ir surface coating (*i.e.* 0.02 mg/cm^2, representing less than 2 % of the total amount of Ir contained in the PEMWE cell) led to stable cell voltage during the slot aging protocol (the 2 nm Ir surface coating degraded during the start-up / shutdown phases). The Au surface coating was shown to be dissolved during the slot aging protocol, and to be redeposited in the PEM or at the anode | PEM interface during the stop events. Finally,

exposure of the uncoated Ti PTL to potentials approaching zero volt limited the contact resistance with the anodic layer, but certainly at the expense of the release of dissolved Ti cations in the membrane electrode assembly. Increasing the clamping stress resulted in an increase of the hydrogen permeation rate and led to a decrease of the contact resistance. Our results also show that the cell performance depends on the history of the clamping: initial tightening to a pressure of 11.2 MPa followed by a loosening led to the best beginning of life performance for our experimental set-up. We argue that the stress relaxation increases the water content of the membrane without affecting the contact resistance.

Acknowledgments

The authors would like to thank the ADEME for funding this study in the frame of the SUPERSTACK project.

References

[1] L. Nikolaos, “FCH JU, Support to Electrolysis in view of 2050 Decarbonisation Targets,” in *ETIP Wind Workshop,Brussels*, Feb. 2019.

[2] M. Carmo, D. L. Fritz, J. Mergel, and D. Stolten, “A comprehensive review on PEM water electrolysis,” *Int J Hydrogen Energy*, vol. 38, no. 12, pp. 4901–4934, Apr. 2013, doi: 10.1016/j.ijhydene.2013.01.151.

[3] M. Möckl *et al.*, “Durability Testing of Low-Iridium PEM Water Electrolysis Membrane Electrode Assemblies,” *J Electrochem Soc*, vol. 169, no. 6, p. 064505, Jun. 2022, doi: 10.1149/1945-7111/ac6d14.

[4] S. Siracusano *et al.*, “New insights into the stability of a high performance nanostructured catalyst for sustainable water electrolysis,” *Nano Energy*, vol. 40, no. April, pp. 618–632, 2017, doi: 10.1016/j.nanoen.2017.09.014.

[5] Y. N. Regmi *et al.*, “Supported Oxygen Evolution Catalysts by Design: Toward Lower Precious Metal Loading and Improved Conductivity in Proton Exchange Membrane Water Electrolyzers,” *ACS Catal*, vol. 10, no. 21, pp. 13125–13135, 2020, doi: 10.1021/acscatal.0c03098.

[6] H. Lv, S. Wang, Y. Sun, J. Chen, W. Zhou, and C. Zhang, “Anode catalyst layer with hierarchical pore size distribution for highly efficient proton exchange membrane water electrolysis,” *J Power Sources*, vol. 564, no. November 2022, p. 232878, 2023, doi: 10.1016/j.jpowsour.2023.232878.

[7] K. A. Lewinski, D. van der Vliet, and S. M. Luopa, “NSTF Advances for PEM Electrolysis - the Effect of Alloying on Activity of NSTF Electrolyzer Catalysts and Performance of NSTF Based PEM Electrolyzers,” *ECS Meeting Abstracts*, vol. MA2015-02, no. 37, pp. 1457–1457, 2015, doi: 10.1149/ma2015-02/37/1457.

[8] M. Bernt and H. A. Gasteiger, “ Influence of Ionomer Content in IrO 2 /TiO 2 Electrodes on PEM Water Electrolyzer Performance ,” *J Electrochem Soc*, vol. 163, no. 11, pp. F3179–F3189, 2016, doi: 10.1149/2.0231611jes.

[9] F. Hegge *et al.*, “Efficient and Stable Low Iridium Loaded Anodes for PEM Water Electrolysis Made Possible by Nanofiber Interlayers,” *ACS Appl Energy Mater*, vol. 3, no. 9, pp. 8276–8284, 2020, doi: 10.1021/acsaem.0c00735.

[10] C. Daiane Ferreira da Silva *et al.*, “Oxygen Evolution Reaction Activity and Stability Benchmarks for Supported and Unsupported IrO $_x$ Electrocatalysts,” *ACS Catal*, vol. 11, no. 7, pp. 4107–4116, Apr. 2021, doi: 10.1021/acscatal.0c04613.

[11] S. Abbou *et al.*, “Manipulating the Corrosion Resistance of SnO_2 Aerogels through Doping for Efficient and Durable Oxygen Evolution Reaction Electrocatalysis in Acidic Media,” *ACS Catal*, vol. 10, no. 13, pp. 7283–7294, Jul. 2020, doi: 10.1021/acscatal.0c01084.

[12] F. Claudel *et al.*, “Degradation Mechanisms of Oxygen Evolution Reaction Electrocatalysts: A Combined Identical-Location Transmission Electron Microscopy and X-ray Photoelectron Spectroscopy Study,” *ACS Catal*, vol. 9, no. 5, pp. 4688–4698, May 2019, doi: 10.1021/acscatal.9b00280.

[13] Z. Xie *et al.*, “MoS2 nanosheet integrated electrodes with engineered 1T-2H phases and defects for efficient hydrogen production in practical PEM electrolysis,” *Appl Catal B*, vol. 313, p. 121458, 2022, doi: 10.1016/j.apcatb.2022.121458.

[14] S. Anwar, F. Khan, Y. Zhang, and A. Djire, “Recent development in electrocatalysts for hydrogen production through water electrolysis,” *Int J Hydrogen Energy*, vol. 46, no. 63, pp. 32284–32317, Sep. 2021, doi: 10.1016/j.ijhydene.2021.06.191.

[15] A. Kusoglu and A. Z. Weber, “New Insights into Perfluorinated Sulfonic-Acid Ionomers,” *Chem Rev*, vol. 117, no. 3, pp. 987–1104, 2017, doi: 10.1021/acs.chemrev.6b00159.

[16] A. Kusoglu *et al.*, “Constitutive response and mechanical properties of PFSA membranes in liquid water,” *J Power Sources*, vol. 195, no. 2, pp. 483–492, 2010, doi: 10.1016/j.jpowsour.2009.08.010.

[17] Y. Tang, A. Kusoglu, A. M. Karlsson, M. H. Santare, S. Cleghorn, and W. B. Johnson, “Mechanical properties of a reinforced composite polymer electrolyte membrane and its simulated performance in PEM fuel cells,” *J Power Sources*, vol. 175, no. 2, pp. 817–825, 2008, doi: 10.1016/j.jpowsour.2007.09.093.

[18] S. Giancola *et al.*, “Composite short side chain PFSA membranes for PEM water electrolysis,” *J Memb Sci*, vol. 570–571, no. August 2018, pp. 69–76, 2019, doi: 10.1016/j.memsci.2018.09.063.

[19] J. Miyake, M. Kusakabe, A. Tsutsumida, and K. Miyatake, “Remarkable Reinforcement Effect in Sulfonated Aromatic Polymers as Fuel Cell Membrane,” *ACS Appl Energy Mater*, vol. 1, no. 3, pp. 1233–1238, 2018, doi: 10.1021/acsaem.7b00349.

[20] X. Zhang, L. Shen, W. Z. Lang, and Y. Wang, “Improved performance of thin-film composite membrane with PVDF/PFSA substrate for forward osmosis process,” *J Memb Sci*, vol. 535, no. April, pp. 188–199, 2017, doi: 10.1016/j.memsci.2017.04.038.

[21] D. Yazili *et al.*, “Sulfonated Poly(Phenylene sulfone) blend membranes finding their way into proton exchange membrane fuel cells,” *J Power Sources*, vol. 563, no. December 2022, 2023, doi: 10.1016/j.jpowsour.2023.232791.

[22] M. Prestat, “Corrosion of structural components of proton exchange membrane water electrolyzer anodes: A review,” *J Power Sources*, vol. 556, p. 232469, Feb. 2023, doi: 10.1016/j.jpowsour.2022.232469.

[23] J. Parra-Restrepo *et al.*, “Influence of the porous transport layer properties on the mass and charge transfer in a segmented PEM electrolyzer,” *Int J Hydrogen Energy*, vol. 45, no. 15, pp. 8094–8106, 2020, doi: 10.1016/j.ijhydene.2020.01.100.

[24] Y. Shi *et al.*, “Understanding the in-plane electron transport in low noble metal proton exchange membrane water electrolyser,” *J Power Sources*, vol. 549, no. July, p. 232130, 2022, doi: 10.1016/j.jpowsour.2022.232130.

[25] M. Bernt, A. Siebel, and H. A. Gasteiger, “Analysis of Voltage Losses in PEM Water Electrolyzers with Low Platinum Group Metal Loadings,” *J Electrochem Soc*, vol. 165, no. 5, pp. F305–F314, Mar. 2018, doi: 10.1149/2.0641805jes.

[26] T. Schuler *et al.*, “Hierarchically Structured Porous Transport Layers for Polymer Electrolyte Water Electrolysis,” *Adv Energy Mater*, vol. 10, no. 2, pp. 1–12, 2020, doi: 10.1002/aenm.201903216.

[27] P. Lettenmeier, S. Kolb, F. Burggraf, A. S. Gago, and K. A. Friedrich, “Towards developing a backing layer for proton exchange membrane electrolyzers,” *J Power Sources*, vol. 311, pp. 153–158, 2016, doi: 10.1016/j.jpowsour.2016.01.100.

[28] Z. Kang *et al.*, “Developing titanium micro/nano porous layers on planar thin/tunable LGDLs for high-efficiency hydrogen production,” *Int J Hydrogen Energy*, vol. 43, no. 31, pp. 14618–14628, 2018, doi: 10.1016/j.ijhydene.2018.05.139.

[29] J. I. Cha, C. Baik, S. W. Lee, and C. Pak, “Improved utilization of IrOx on Ti4O7 supports in Membrane Electrode Assembly for Polymer Electrolyte Membrane Water Electrolyzer,” *Catal Today*, no. August 2021, pp. 1–9, 2022, doi: 10.1016/j.cattod.2022.01.015.

[30] C. Rakousky, U. Reimer, K. Wippermann, M. Carmo, W. Lueke, and D. Stolten, “An analysis of degradation phenomena in polymer electrolyte membrane water electrolysis,” *J Power Sources*, vol. 326, pp. 120–128, 2016, doi: 10.1016/j.jpowsour.2016.06.082.

[31] C. Liu *et al.*, “Exploring the Interface of Skin-Layered Titanium Fibers for Electrochemical Water Splitting,” *Adv Energy Mater*, vol. 11, no. 8, 2021, doi: 10.1002/aenm.202002926.

[32] C. Liu *et al.*, “Degradation Effects at the Porous Transport Layer/Catalyst Layer Interface in Polymer Electrolyte Membrane Water Electrolyzer,” *J Electrochem Soc*, 2023, doi: 10.1149/1945-7111/acc1a5.

[33] S. Stiber *et al.*, “A high-performance, durable and low-cost proton exchange membrane electrolyser with stainless steel components,” *Energy Environ Sci*, vol. 15, no. 1, pp. 109–122, 2022, doi: 10.1039/d1ee02112e.

[34] N. F. Daudt, A. D. Schneider, E. R. Arnemann, C. J. Scheuer, L. S. Dorneles, and L. F. Schelp, “Fabrication of NbN-Coated Porous Titanium Sheets for PEM Electrolyzers,” *J Mater Eng Perform*, vol. 29, no. 8, pp. 5174–5183, 2020, doi: 10.1007/s11665-020-05026-y.

[35] A. Martin *et al.*, “Communication—Proving the Importance of Pt-Interlayer Position in PEMWE Membranes for the Effective Reduction of the Anodic Hydrogen Content,” *J Electrochem Soc*, vol. 168, no. 9, p. 094509, 2021, doi: 10.1149/1945-7111/ac275b.

[36] C. Y. Wen, Y. S. Lin, and C. H. Lu, “Experimental study of clamping effects on the performances of a single proton exchange membrane fuel cell and a 10-cell stack,” *J Power Sources*, vol. 192, no. 2, pp. 475–485, 2009, doi: 10.1016/j.jpowsour.2009.03.058.

[37] P. Zhou, C. W. Wu, and G. J. Ma, “Influence of clamping force on the performance of PEMFCs,” *J Power Sources*, vol. 163, no. 2, pp. 874–881, 2007, doi: 10.1016/j.jpowsour.2006.09.068.

[38] S. Al Shakhshir, X. Cui, S. Frensch, and S. K. Kær, “In-situ experimental characterization of the clamping pressure effects on low temperature polymer electrolyte membrane electrolysis,” *Int J Hydrogen Energy*, vol. 42, no. 34, pp. 21597–21606, 2017, doi: 10.1016/j.ijhydene.2017.07.059.

[39] S. H. Frensch, A. C. Olesen, S. S. Araya, and S. K. Kær, “Model-supported characterization of a PEM water electrolysis cell for the effect of compression,” *Electrochim Acta*, vol. 263, pp. 228–236, 2018, doi: 10.1016/j.electacta.2018.01.040.

[40] O. F. Selamet and M. S. Ergoktas, “Effects of bolt torque and contact resistance on the performance of the polymer electrolyte membrane electrolyzers,” *J Power Sources*, vol. 281, pp. 103–113, 2015, doi: 10.1016/j.jpowsour.2015.01.162.

[41] E. Borgardt *et al.*, “Mechanical characterization and durability of sintered porous transport layers for polymer electrolyte membrane electrolysis,” *J Power Sources*, vol. 374, no. November 2017, pp. 84–91, 2018, doi: 10.1016/j.jpowsour.2017.11.027.

[42] E. Borgardt *et al.*, “Impact of clamping pressure and stress relaxation on the performance of different polymer electrolyte membrane water electrolysis cell designs,” *Int J Hydrogen Energy*, vol. 44, no. 42, pp. 23556–23567, 2019, doi: 10.1016/j.ijhydene.2019.07.075.

[43] J. Mahan, *Physical Vapor Deposition of Thin Films*. 2000.

[44] *X-ray and Neuron Reflectivity: Principles and Applications*, vol. 58. Berlin, Heidelberg: Springer Berlin Heidelberg, 1999. doi: 10.1007/3-540-48696-8.

[45] J. parra restrepo LEMTA, “Docteur de L ’ Université de Lorraine Caractérisation des hétérogénéités de fonctionnement et de dégradation au sein d ’ un électrolyseur à membrane échangeuse de protons (PEM),” 2020.

[46] S. Kim, A. A. Polycarpou, and H. Liang, “Electrical-potential induced surface wettability of porous metallic nanostructures,” *Appl Surf Sci*, vol. 351, pp. 460–465, Oct. 2015, doi: 10.1016/j.apsusc.2015.05.148.

[47] J. Lee, H. Moon, J. Fowler, T. Schoellhammer, and C.-J. Kim, “Electrowetting and electrowetting-on-dielectric for microscale liquid handling,” *Sens Actuators A Phys*, vol. 95, no. 2–3, pp. 259–268, Jan. 2002, doi: 10.1016/S0924-4247(01)00734-8.

[48] E. McCafferty, “Thermodynamics of Corrosion: Pourbaix Diagrams,” in *Introduction to Corrosion Science*, New York, NY: Springer New York, 2010, pp. 95–117. doi: 10.1007/978-1-4419-0455-3_6.

[49] J. J. Noël, “The Electrochemistry of Titanium Corrosion,” University of Manitoba, 1999.

[50] S. Cherevko *et al.*, “Dissolution of Platinum in the Operational Range of Fuel Cells,” *ChemElectroChem*, vol. 2, no. 10, pp. 1471–1478, Oct. 2015, doi: 10.1002/celc.201500098.

[51] A. A. Topalov *et al.*, “Dissolution of Platinum: Limits for the Deployment of Electrochemical Energy Conversion?,” *Angewandte Chemie International Edition*, vol. 51, no. 50, pp. 12613–12615, Dec. 2012, doi: 10.1002/anie.201207256.

[52] S. Cherevko, S. Geiger, O. Kasian, A. Mingers, and K. J. J. Mayrhofer, “Oxygen evolution activity and stability of iridium in acidic media. Part 2. – Electrochemically grown hydrous iridium oxide,” *Journal of Electroanalytical Chemistry*, vol. 774, pp. 102–110, Aug. 2016, doi: 10.1016/j.jelechem.2016.05.015.

[53] C. Rakousky *et al.*, “Polymer electrolyte membrane water electrolysis: Restraining degradation in the presence of fluctuating power,” *J Power Sources*, vol. 342, pp. 38–47, Feb. 2017, doi: 10.1016/j.jpowsour.2016.11.118.

[54] S. Lædre, O. E. Kongstein, A. Oedegaard, H. Karoliussen, and F. Seland, “Materials for Proton Exchange Membrane water electrolyzer bipolar plates,” *Int J Hydrogen Energy*, vol. 42, no. 5, pp. 2713–2723, Feb. 2017, doi: 10.1016/j.ijhydene.2016.11.106.

[55] D. J. Blackwood, L. M. Peter, and D. E. Williams, “Stability and open circuit breakdown of the passive oxide film on titanium,” *Electrochim Acta*, vol. 33, no. 8, pp. 1143–1149, Aug. 1988, doi: 10.1016/0013-4686(88)80206-8.

[56] M. Milosevic *et al.*, “In Search of Lost Iridium: Quantification of Anode Catalyst Layer Dissolution in Proton Exchange Membrane Water Electrolyzers,” *ACS Energy Lett*, vol. 8, no. 6, pp. 2682–2688, Jun. 2023, doi: 10.1021/acsenergylett.3c00193.

[57] Fabien Claudel, “https://www.theses.fr/241705568 .”

[58] T. Sakai, H. Takenaka, N. Wakabayashi, Y. Kawami, and E. Torikai, “Gas Permeation Properties of Solid Polymer Electrolyte (SPE) Membranes,” *J Electrochem Soc*, vol. 132, no. 6, pp. 1328–1332, Jun. 1985, doi: 10.1149/1.2114111.